Anisotropic atom displacement in Pd nanocubes resolved by molecular dynamics simulations supported by x-ray diffraction imaging

P. Scardi, A. Leonardi, L. Gelisio, M. R. Suchomel, B. T. Sneed, M. K. Sheehan, and C.-K. Tsung

Phys. Rev. B **91**, 155414 — Published 14 April 2015

DOI: 10.1103/PhysRevB.91.155414

Anisotropic atom displacement in Pd nanocubes resolved by MD simulations supported by XRD imaging

P. Scardi,[1,*] A. Leonardi,[1] L. Gelisio,[1] M.R. Suchomel,[2]
B.T. Sneed,[3] M.K. Sheehan,[3] and C.-K. Tsung[3]

[1] *University of Trento, Department of Civil, Environmental & Mechanical Engineering, via Mesiano 77, Trento 38123, Italy*

[2] *Advanced Photon Source, 9700 S. Cass Ave. Argonne National Laboratory, Argonne, IL 60439, USA*

[3] *Boston College, Merkert Chemistry Center, Department of Chemistry, 2609 Beacon St., Chestnut Hill, MA 02467, USA*

(Dated: April 2, 2015)

Abstract

Nearly identical Pd nanocubes yield an X-ray powder diffraction pattern with interference fringes affording access to unprecedented structural details of nanocrystal size, shape, and complex atomic displacement for a billion-sized population. The excellent agreement between diffraction data and molecular dynamics (MD) provides strong experimental validation of MD simulations and the proposed data-interpretation paradigm. These results show that individual atomic displacements within the nanocubes are not only a function of disrupted bonds and the crystallographic plane of the adjacent surface; rather complex strain gradients extending across all surfaces of the particle strongly influence atomic displacements. This observation of non-uniform surface strain and the manner in which it is affected by different sizes, shapes, and locations within each facet could be the key to understand many surface related properties of shaped nanocrystals including those associated with important catalysis applications.

Keywords: Pd nanocrystals, catalysts, X-ray diffraction, Molecular Dynamics, local atomic displacement, strain anisotropy

Morphology is the most commonly sought after characteristic of nanocrystals, especially when coupled to property maps of surface strain and chemical composition. This information is critical to many research fields and is particularly important for understanding catalytic reactivity. Catalytic processes contribute in some way to more than one third of global GDP, and heterogeneous catalysis on metal surfaces constitutes a large portion of this industry, facilitating the chemical production of common products, *e.g.* ammonia, hydrogen from steam reforming of natural gas, and reduced CO emissions in automotive exhaust.[1]

Since the first classical demonstrations of morphology-controlled colloidal nanocrystals,[2] a great effort has been made to understand morphology-dependent catalysis processes.[3–9] It is not straightforward to assess this dependence because the actual arrangement of atoms within shaped nanocrystals is more complex than the traditional polyhedral model crystals envisaged. Compressed or expanded atomic arrangements arise from the high energy of under-coordinated atoms at the surfaces, edges, and vertices. It is important to resolve these non-idealized atom arrangements, as the surface electronic structure directly influences the binding energies of adsorbates, intermediates, and products along reaction pathways on catalytic surfaces.[10–15]

A complete resolution of atomic arrangements within nanocrystals at a global aggregate scale will drive progress in fundamental and applied nanocrystal research. Electron microscopy has made great strides along this direction,[16] supported by the development of aberration-corrected scanning transmission electron microscopy (TEM) and high angle annular dark field imaging (HAADF).[17–24] While state-of-the-art microscopy delivers the highest spatial resolution of any probe, showing features down to the atomic scale, the statistical basis is limited by a low sampling. It is typical that only a handful of "representative" nanocrystals are to be examined in an electron microscope, before projecting this selected ideal on the rest of the batch, which contains several billions of other uncharacterized particles.[18,25] Furthermore, the electron beam can damage the samples and make *in-situ* measurements challenging.

Considerable insights of atomic arrangements may also be obtained by coherent X-ray diffraction (CXD), a powerful imaging technique that provides morphological information together with a spatially resolved map of lattice strain. However, the smallest nanocrystals which can be studied by CXD using currently available instruments are about 60nm in diameter.[26] Smaller crystalline sizes create considerable and still unsolved challenges in terms

of counting statistics for the experimental CXD pattern.

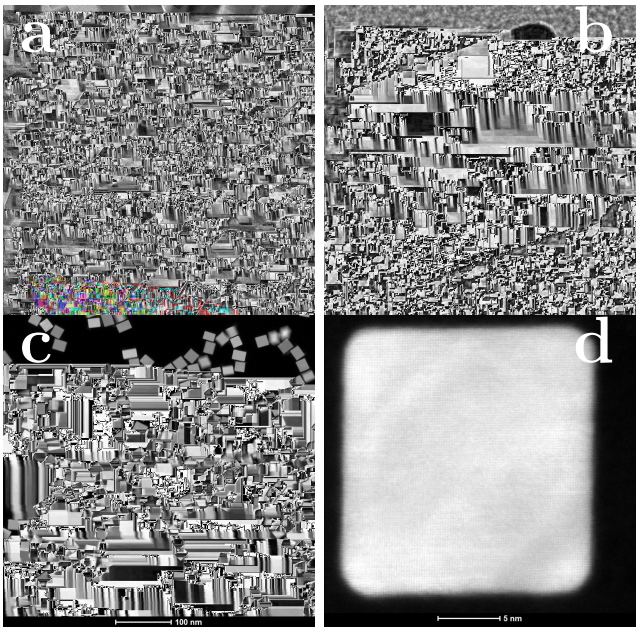

FIG. 1. TEM (a,b) and HAADF (c,d) images of Pd nanocrystals. (b,d) A nanocrystal oriented along [00h], showing the truncation of edges and corners responsible for (110) and (111) faceting, respectively. The fraction of non-cubic atomic aggregates was estimated to be approximately 1.5% in number, corresponding to a negligible fraction of the sample volume ($\ll 1\%$).

It may appear non-intuitive that the traditional and established technique of X-ray powder diffraction (XRPD) should enter the picture at this stage. Besides revealing the average phase composition, XRPD is routinely used to assess the size of nanocrystals: quick estimates are obtained from the peak width, exploiting the inverse proportionality with the domain size stated by the Scherrer equation, frequently ignoring effects of the specific nanocrystal shape, defects, and lattice distortions.[19] This paradigm could change dramatically with the current trend of nanotechnology toward a better control of synthesis conditions, aimed at producing nanocrystals with identical size and shape. Under these conditions XRPD can offer detailed information similar to that afforded by an imaging technique like CXD, with additional advantages such as of incorporating the ensemble of peaks produced by billions of nanocrystals in a typical specimen offering inexpensive data collection, and straightforward analysis.

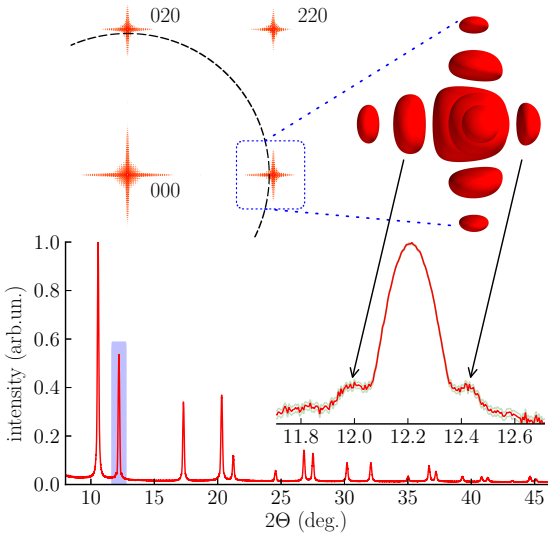

FIG. 2. Experimental X-ray powder pattern for the studied Pd nanocrystals. The inset shows a detail of the (200) peak. Arrows on the latter indicate the interference fringes from the parallel 100 facets of the nanocrystals, which correspond to the analogous features observed in Reciprocal Space (above): powder diffraction integrates information over spheres of growing radius in RS, as schematically represented in the inset of the upper figure.

I. RESULTS

This new paradigm is demonstrated here for cubic palladium nanocrystals, a typical system in catalytic applications.[6,7,27] As shown in Fig.1, we produced nearly identical cubic-shape nanocrystals; a closer look reveals that edges and corners are truncated, so the external shape is not framed by (100) planes only, but includes fractions of (110) (edge) and (111) (corner) planes. The XRPD pattern collected at the 11-BM beamline of the APS synchrotron radiation facility, using a standard capillary (Debye-Scherrer) geometry at room temperature, gives a unique fingerprint.

This is highlighted in the inset of Fig.2, where the 200 reflection shows interference fringes from the parallel 100 facets, a feature specific to cubic crystals, which is observable here because the nanocrystals are nearly identical in size and shape. This evidence parallels the typical information produced on much larger cubic crystals by CXD with the same pattern modulation along <h00> directions.[28] In addition, the XRPD pattern provides information

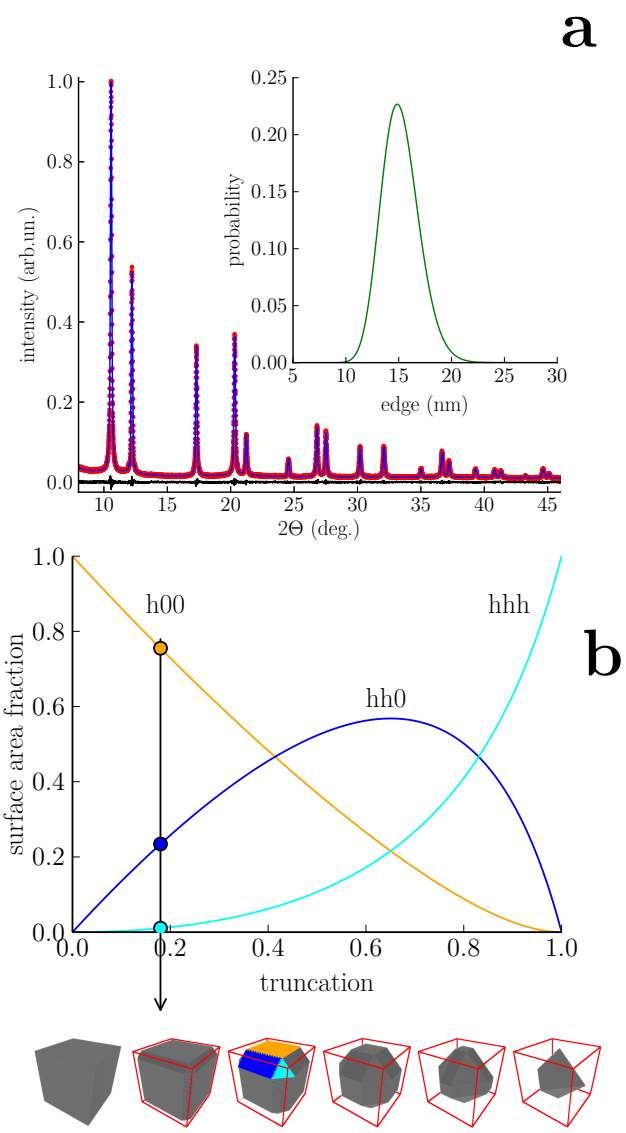

FIG. 3. Modeling (line) of the X-ray powder diffraction data of Fig.2 (dot), together with residual (line below). The resulting distribution of cube edges is shown in the inset (a). Diffraction data modeling also provides the best value of cube truncation, on a scale ranging from cube (0% truncation) to octahedron (100% truncation). As shown by the pictures, truncation involves different extension of exposed (100), (110) and (111) facets (surface area fraction in the plot) (b). Refined unit cell parameter is $a_0 = 0.38900(2)$nm, and Debye-Waller factor, $B_{iso} = 6.4(1)\,10^{-3}$nm^2.

along multiple crystallographic directions, which can be used to model the entire pattern. In particular, we can implement a truncated edge and corner cube model to refine the level of cube edge and corner truncation, and distribution of sizes.[29]

The result in Fig.3 shows the remarkably good match between model and data, with nanocrystal size and shape determined from XRPD modeling in good agreement with TEM. According to the data modeling, nanocubes have edges of 15nm, with a standard deviation of 2nm, and an edge/corner truncation of 18%, on a scale ranging from perfect cube (0%) to octahedron (100%).

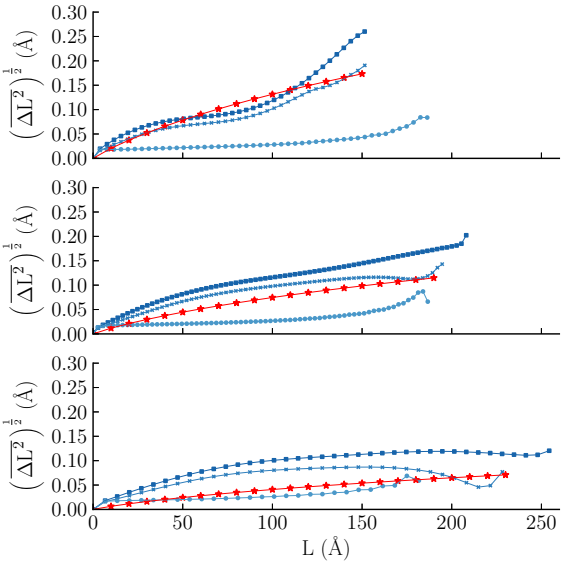

FIG. 4. Warren's plot for the studied system: root-mean-square atomic displacement along the given scattering direction (upper figure, [h00], center figure, [hh0], lower figure, [hhh]) as a function of the correlation distance L between scattering centers within the crystalline domain. The trends shown refer to results of the modeling of the experimental XRPD data (★) and to MD results for a perfect cube (■), a truncated cube as that described in Fig. 3 and 4 (×), and a sphere (•), all of them with the same total number of atoms (or volume).

The XRPD modeling also includes strain effects, described according to elastic tensor symmetry (cf Methods), which capitalize on hkl-dependent line broadening information to probe strain anisotropy ($S_2 = 0.00018(4)$, $B = -2.6(1)$, $a = 1.04(8)\,10^{-5}$, $b = 7.0(1)\,10^{-7}$, see Methods for details). The result is shown in a Warren's diagram,[30] representing the standard deviation of the atomic displacement distribution as a function of the distance L between scattering centers along each given crystallographic orientation. Examples of these diagrams are shown in Fig.4 for three directions, [hhh], [hh0] and [h00], with the first and last corresponding to the extremes of anisotropic elastic behavior. The r.m.s. displacement

is larger along [h00], *i.e.* perpendicular to the cube faces, than along [hhh], *i.e.* the body diagonal direction. This is not only a direct consequence of the elastic anisotropy of Pd, but is also related to the shape of the nanocrystal.

To better appraise the relevance of these results, the truncated edge/corner cube suggested by Fig.3 was used to create an atomistic model. Molecular dynamics (MD) was used to generate a plausible representation of the Pd nanocrystals at room temperature. As a result of the MD procedure, driven by the reduction of potential energy of the crystal, atoms are displaced from their reference positions. The effect is especially evident in surface regions. An example of this displacement field, calculated with respect to the corresponding ideal fcc lattice, is shown in Fig.5a for a (100) face and adjacent (110) and (111) facets (defined with respect to the refined truncated cube shape of Fig.3). Corner atoms have the highest tendency to shrink toward the core, with the overall effect that the nanocrystal surface is bent outward, as if tending towards a spherical shape.

The atomic-level information provided by MD can be used to calculate Warren's plots along specific crystallographic directions, to compare the trends with those obtained experimentally by XRPD. This comparison between a modeled sphere shape, a perfect cube with sharp edges and cube with truncated edges and corners suggested by the XRPD analysis is shown in Fig.4. The agreement with the XRPD result is reasonably good, considering the difference between the two methods, and the fact that the XRPD modeling enforces a smooth (linear to square root) trend with L, the correlation length between couples of scattering centers in the crystalline domain. The Warren plot strain profiles calculated by MD display differences associated with each particle shape, and the overall agreement between the truncated cube model and XRPD experimentally derived curve reveals the high sensitivity of this analysis technique to subtle particle shape details like edge truncation.

To better assess the relevance of nanocrystal shape, the same figure shows Warren's plots for a spherical Pd nanocrystal with the same number of atoms. Atomic displacements in a spherical object are much smaller, and the overall shrinking effect much more isotropic than in the cubic nanocrystals. The symmetry of the spherical shape tends to cancel out different displacement components arising from the elastic anisotropy of Pd. As an additional valence of the results of Fig.4, the good match with the XRPD trends provides a strong experimental validation for the MD simulations, so far hardly available in the literature on this specific subject. MD predictions can then be safely used to further speculate about the nature of

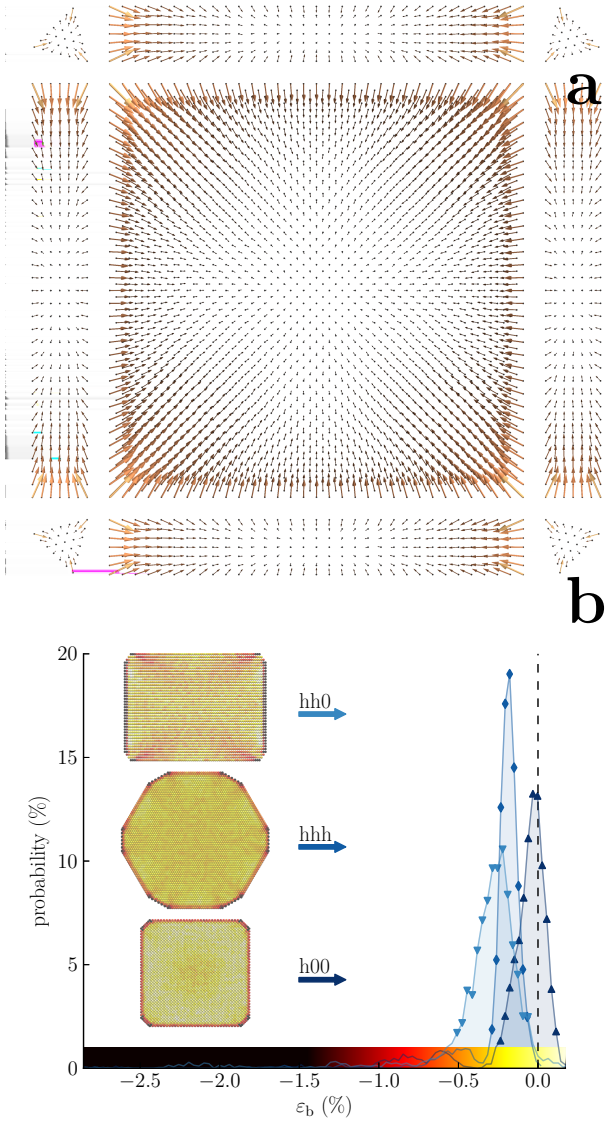

FIG. 5. Map of atomic displacement from the starting (ideal) positions to equilibrium after MD on (100), (110) and (111) facets for the cubic nanocrystal with truncation of edges and corners as from the XRPD results; arrows are amplified for graphical convenience (a); histogram of the average local strain (see Methods) on three significant cross-sections (hh0), (hhh) and (h00), shown in the inset. The color scale shown on the abscissa represents the strain distribution (b).

strain in metal nanocrystals. With this capability, we are able to generate a more accurate picture of lattice strain, which can be coupled to other property maps. Fig.6 shows a TEM image of some representative Pd nanocrystals, with corresponding displacement maps calculated by MD. The out-of-plane (normal) displacement component (top) is highest in face center regions, pushing atoms outward, and along all edges, with opposite, strong

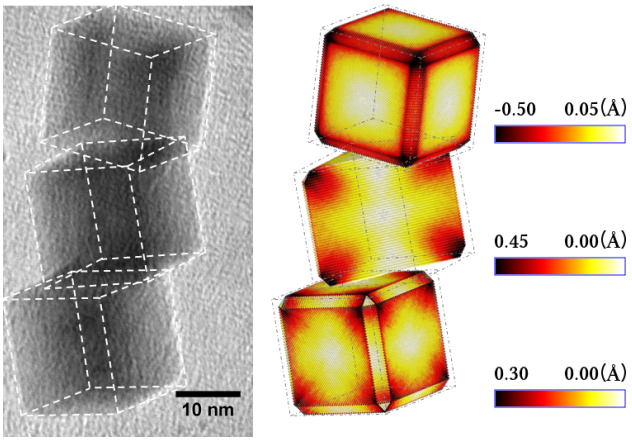

FIG. 6. TEM picture of Pd nanocubes (left, dash is drawn just to drive the eye) with corresponding atomic displacement maps (right) for: normal component on the surface (top), norm of the component projected on the (110) cross-section (middle), and on the surface of the nanocrystal (bottom). Details and definitions are reported in the Methods.

inward displacement. This is responsible for the curvature of atomic facets, which has been experimentally observed in similar systems.[31] All displacement components tend of course to build up from core to surface, a feature visible in the (110) cross-section map (center): inward displacement is highest along body diagonal, whereas a broad, roughly pyramidal region has atoms displaced outward, along the [h00] directions. It is also worth studying the atomic displacement in the plane of each exposed facet (lower cube). Here one clearly see the component projected on the surface, which tends to be the highest near corners and edges (dark regions) and is lower in the center of each facets (light-color regions): most importantly, the pattern is far from being uniform on each given facet.

II. DISCUSSION

Our new observation of anisotropic atomic displacement in shaped nanocrystals can be used to explain and support many unique results in morphology-dependent catalysis previously reported in the literature. The relationship between shape, strain, and catalytic behavior can be invoked for nanocrystal-catalyzed hydrogenations[3,8,9] and electrocatalysis relevant to energy conversion chemistry.[6,23,32–34] For example, one representative work reported recently by Laskar *et al.*[7] studied selective hydrogenation of alkynes on shaped Pd

nanocrystals. Similar to many previous reports, their study on Pd cubes of different sizes showed that catalytic activities, when normalized by the surface area, are higher for larger sized nanocrystals. It was reasoned that the increased ratio of face atoms to corner and edge atoms increased the number of active sites available *via* an ensemble effect. This conjecture is based on a previous work that suggests the phenomenon has a threshold around 11nm, beyond which the effect would be non-existent.[35] However, the variation in ratios of face atoms to edge and corner atoms at the larger size ranges encountered by Laskar *et al.*[7] are quite small (ranging between 98-99% face atoms); and so it is unlikely that such an increase in the catalytic performance is influenced by ensemble effects alone. Both size-dependent anisotropic displacement of constituent atoms within the particle plays a role at these nano size scales (10-40nm), as well as non-uniform distributions of atomic distances across the exposed facets. Furthermore, the displacement would have a considerable impact on the geometry of the proposed ensemble sites. These two effects, site availability and geometry, could be coupled cooperatively, increasing catalytic activities for larger sizes.

This important feature is shown in Fig.7a, where histograms of the average local strain (ε_b) on the (100) face are compared for different particle sizes. Two main features are clearly shown by the distributions: a peak located approximately at $\varepsilon_b \approx -1.25\%$ (peak E) and another one, larger and closer to zero (peak I). Peak E is related to atoms along the edges of the (100) facet, whereas peak I belongs to atoms sitting inside the face. The inset shows trends of mean ε_b values and standard deviation of peak I: for increasing nanocrystal size, peak I moves toward zero-strain values, *i.e.*, toward the equilibrium bond length (0.389nm in these simulations).At the same time the standard deviation tends to slightly decrease, as the strain becomes more homogeneous across the (100) surface. This result clearly indicates that the average local strain on (h00) facets is largest in smallest cubes, and increasingly more uniform for larger sizes.

Besides the size-dependent non-uniformity, nanocrystal shape also has a direct effect on the displacement. This is shown in Fig. 7b, where the average local strain histograms refer to nanocrystals with the same total surface area, but enclosed by different facets, respectively, (hhh) for octahedron, (h00) for cube, and (hh0) for rhombic dodecahedron. The cubic shape gives the largest dispersion of strain values, whereas the octahedral shape has more uniform surface strain, and the (hh0) surface enclosed shape is in between. This shape-dependent atom displacement information was not precisely factored into the analysis

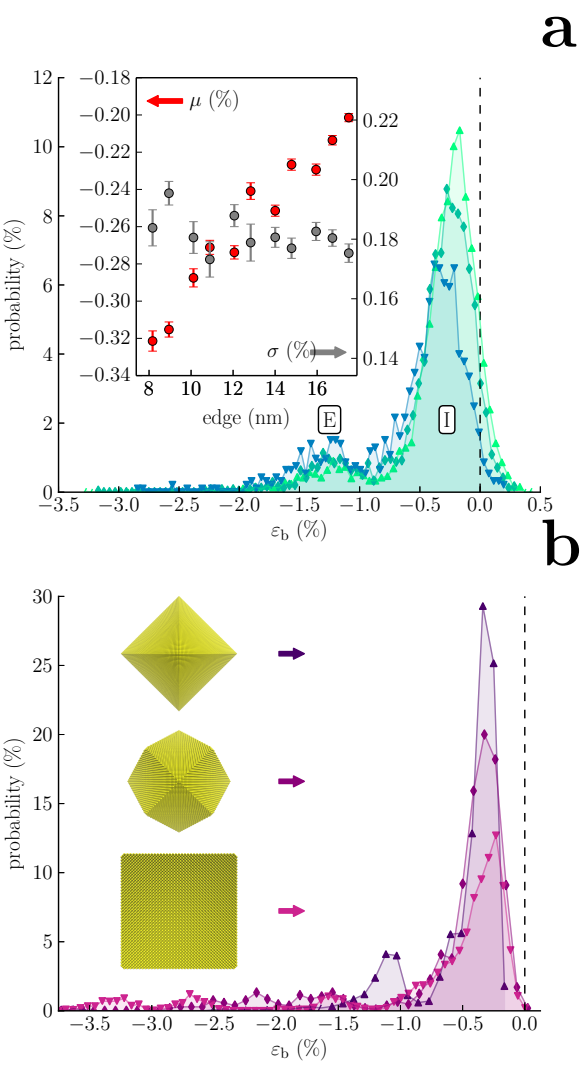

FIG. 7. Histogram of the average local strain (see Methods): (a) on (100) face for three different sizes (same shape, *i.e.*, the truncated cube resulting from the XRPD analysis, and 8.2 (▼), 13.2 (♦), and 18.3 (▲) nm edge, respectively 70,139, 290,407 and 758,655 atoms); the inset shows mean position and width (standard deviation) of the main strain component. (b) nanocrystals with same total surface, enclosed by different facets: octahedron (hhh), rhombic dodecahedron (hh0), and cube (h00), respectively 281,275, 268,345 and 228,259 atoms.

of catalytic performance of shaped nanocrystals. While most works cite that the different packing of atomic planes results in changes to catalytic behaviors, the strained surface that exists due to the displacement likely contributes as well.[3,8,9] It is worth considering that even slight adjustments to the d-band structure (sorption characteristics) of a catalyst for a particular reaction, which may involve multiple intermediates and mechanistic pathways, can

have a significant impact. Changes in d-band structure from strain can result in unexpected behavior, where both tensile and compressive strain can give similar d-band shifts and activity increases.[36]

We believe the surface strain in these (and other) nanostructures could be responsible for both their improved performance and selectivity, and the combination of experiment and simulation presented here allows for a technique to assess and predict this strain influence on catalysis. This critical information, previously unavailable to scientists, can now be acquired and incorporated into theory to paint a more complete and global picture of catalysis on metal nanoparticle surfaces.

III. METHODS

A. Synthesis of the Pd nanocubes

Pd nanocubes were synthesized by adapting a procedure from the literature.[27] Typically, 105mg of polyvinylpyrrolidone (PVP, MW: ≈40,000), 600mg of potassium bromide (KBr, 99%), and 60mg of L-ascorbic acid (99%) were first dissolved in a ≈20mL glass scintillation vial in a total volume of 8.0mL of deionized water (18.2MΩ). This was then placed in an oil bath set to 373K to equilibrate for approximately 10 minutes with stirring at a rate of 500rpm. Meanwhile, a separate solution was created containing 57mg sodium tetrachloropalladate (Na_2PdCl_4, 99%) dissolved in 3.0mL of deionized water. This was then rapidly injected into the previously prepared solution. The vial was capped and the reaction was allowed to continue for 3 hours before removing from the oil bath. The particles were concentrated and collected via precipitation by adding acetone to the solution in a 10:1 acetone:water ratio and centrifuging at 8,000rpm. The particles were then rinsed and brought down twice more in the same manner before being redispersed in 100μL water as the final volume of solution used for the preparation of TEM and XRD experiments.

B. Characterization of the Pd nanocubes

For imaging by TEM, 15μL droplets were dropcast onto a carbon-coated copper grid, or alternatively, 1μL of the nanoparticle dispersion was placed on a grid and allowed to dry in air. A JEOL JEM2010F was the instrument used, operated at 200kV. For analysis by

high resolution X-ray Diffraction (XRD), 20μL of the concentrated nanoparticle dispersion was slowly injected into Kapton tubes, ≈2-3cm in length and 0.80mm in diameter, using a microsyringe. The tubes were then allowed to dry for a few days before being sealed with epoxy.

The XRD data were collected at 11-BM, the powder diffraction beamline of Argonne National Laboratory (Advanced Photon Source). The capillary was then mounted on the 11-BM spinner, operated at 4,200rpm, to improve statistics and uniformity. Two subsequent measurements of one hour each were made at room temperature (298K), with a wavelength of 0.0413874nm (≈30keV) in the standard Debye-Scherrer geometry, over a 2Θ range from 0° to 60°, using a detector system based on 12 independent Si(111) analyzers. The 2Θ sampling step was 0.005°, with a counting time of 0.3s per step. In addition to the XRD measurements, after aligning the detector with the X-ray beam and removing the beam stopper, the transmitted signal through the sample was collected while the capillary moved across the beam; this way sample absorption could be assessed, resulting in a fractional intensity decrease of 0.026 (i.e., the transmitted beam fraction is $I/I_0 = 0.974$), sufficiently low to make any correction for the absorption effect unnecessary.

C. X-ray diffraction data analysis

The XRD data were analyzed by whole powder pattern modeling.[37] Based on the concept of Common Volume Function,[29] crystalline domains were described as cubes with truncated edges and triangular corners, with a refinable parameter to determine the truncation (from 0 for perfect cube to 1 for a complete truncation, resulting in an octahedron). Dispersion of sizes was accounted for by refining mean and variance of a lognormal distribution of cube edge lengths. The average crystal structure ($Fm\overline{3}m$) of Pd was implemented to calculate the integrated intensities of the Bragg peaks. Besides the traditional Debye-Waller factor (B_{iso}), the modeling also included temperature diffuse scattering (TDS), according to a recently developed procedure for nanocrystalline domains.[38] As shown in the cited reference, for most fcc materials this procedure does not require additional parameters other than B_{iso}. The instrumental profile, which is a very well known and characterized function for the 11-BM beamline, was described in parametric form (as a function of the 2Θ angle), based on the experimentally measured line profile standard (NIST SRM-660b, LaB_6).

Strain effects were described according to the symmetry of the elastic tensor, and in particular with the fourth order invariant form of Miller indices for cubic materials[39]

$$\Gamma_{hkl} = A + B\frac{h^2k^2 + k^2l^2 + l^2h^2}{\left(h^2 + k^2 + l^2\right)^2} = A + BH^2. \quad (1)$$

The main effect is an additional, *hkl*-dependent line broadening which can be described in terms of strain distribution. This distribution can be represented by a Voigt curve, *i.e.*, a convolution of Lorentzian and Gaussian functions, so that the Fourier Transform (FT) of the peak profile component related to strain effects can be written as[39,40]

$$A^D\left(L\right) = \exp\left[-q^2L^2\overline{\varepsilon^2_{hkl}\left(L\right)}/2\right] \cong \exp\left[-q^2\Gamma_{hkl}\left(aL + bL^2\right)/2\right], \quad (2)$$

where q ($= 4\pi\sin\left(\Theta\right)/\lambda$) is the modulus of the wavevector transfer, and $\overline{\varepsilon^2_{hkl}\left(L\right)}$ is the variance of the strain distribution for a correlation (or Fourier) length L; the latter spans from zero (selfcorrelation) to the longest distance in the crystalline domain along the considered [hkl] direction.

As an additional minor effect, peak positions are also slightly displaced by the lattice distortion, and the effect can be related to interplanar spacing, d_{hkl}, as[41]

$$d_{hkl} = d^0_{hkl}\left(S_1 + S_2H^2\right). \quad (3)$$

S_1, S_2 are refinable parameters, whereas d^0_{hkl} is obtained from the refined unit cell parameter (a_0) using the Bragg's law.

When using equations (2) and (3), A can be fixed to unity and S_1 to zero, while B, a, and b and S_2 are treated as free, refinable parameters. This strategy reduces the number of free parameters and correlations among them, with no significant effect on the results. Correlations are relatively weak, as B, a, and b are related to the inhomogeneous strain component and influence peak width and shape, whereas S_2 is related to the average strain which affects the peak position.[42]

Fourier Transforms of all contributing effects (CVF, which in normalized form is the FT of the size/shape profile component; instrumental component in parametric form; equation (2) for the strain effect) were multiplied and, by the convolution theorem of FTs, used to model the experimental data. Details on the procedure can be found elsewhere.[37]

A convenient way to represent the local atomic displacement is by the Warren's plot, originally introduced in research studies on plastically deformed metals.[30] The plot reports

the atomic displacement in terms of standard deviation of the displacement distribution, $\sqrt{\overline{\Delta L_{hkl}^2(L)}} = L\sqrt{\overline{\varepsilon_{hkl}^2(L)}}$, as a function of L. Once the free parameters in equation (2) have been determined by modelling the experimental peak profiles, Warren's plots for any desired [hkl] scattering direction can be obtained in a simple and straightforward way.

D. Atomistic simulations

Particles were carved out of an ideal fcc lattice ($a_0 = 0.389$nm), the shape mimicking objects portrayed in HRTEM pictures (*as-built* objects hereinafter), with edge/corner truncation as from the XRD analysis. Physically-sound atomic configurations were obtained by Molecular Dynamics (MD) using the Large-scale Atomic/Molecular Massively Parallel Simulator (LAMMPS).[43] The atomic interaction was based on the Embedded Atom Method (EAM)[44–46] and the integration timestep (1.5fs) was set to one-hundredth of the reciprocal of the largest (bulk) phonon frequency (6.48THz, according to[46]) at room temperature ($RT = 298.150$K). Number of atoms ($N = 234,311$), Volume ($V = 23.34$ nm^3) of the system and Temperature ($T = RT$) were kept constant (*i.e.* canonical ensemble: constant N, V and T) until an appropriate equilibrium were reached ($250,000$ steps, $0.3750ns$) employing Langevin dynamics (using a damping parameter of $2.5ps$)[47] and then a chain of Nosè-Hoover thermostats (5.0ps as damping parameter and implementing the MTK correction).[48] At a later stage, the constraint on T was removed and the simulations were performed in the (microcanonical) NVE ensemble. During this stage atomic coordinates were dumped every 1,000 steps along the MD trajectory (500 frames). To remove the effect of atomic vibrations, this set of frames was then time-averaged (*time-averaged* objects hereinafter) so to single out the static displacement field.

Given the position of the i-th atom in the *as-built* configuration ($\vec{r}_{i,ab}$) and in the *time-averaged* one ($\vec{r}_{i,ta}$), the displacement vector is given by

$$\vec{\Delta}_i = \vec{r}_{i,ta} - \vec{r}_{i,ab}. \tag{4}$$

This simple quantity allows for an immediate (although qualitative) visual perception of the deviation from the reference structure. Given a plane described by its normal versor $\hat{n}$, the above quantity can be projected on the plane,

$$\mathrm{P}_{\hat{n}}\left(\vec{\Delta}_i\right) = \vec{\Delta}_i - \left(\vec{\Delta}_i \cdot \hat{n}\right)\hat{n} \tag{5}$$

and normal to the plane,

$$\mathrm{R}_{\hat{n}}\left(\vec{\Delta}_i\right) = \left(\vec{\Delta}_i \cdot \hat{n}\right)\hat{n}, \tag{6}$$

so that $P_{\hat{n}}\left(\vec{\Delta}_i\right) + \mathrm{R}_{\hat{n}}\left(\vec{\Delta}_i\right) = \vec{\Delta}_i$. To provide a quantitative picture of atomic level displacement, the average bond length of each atom is considered. In the *as-built* configuration, Z_i neighbors of atom i are identified by drawing an annulus centered on the given atom, with mean radius equal to the first neighbors distance ($a_0/\sqrt{2} = 0.2751nm$), and lying on the plane described by the normal versor $\hat{n}$. The neighbor list computed in the previous step is used to draw the vector connecting atom i to its neighbor j, $\vec{r}_{ij} = \vec{r}_i - \vec{r}_j$, which is then used to compute the average bond length (the Euclidean norm of the above-defined vector),

$$b_i = \frac{1}{Z_i}\sum_{j=1}^{Z_i}\|\vec{r}_{ij}\|. \tag{7}$$

The quantity

$$\varepsilon_{b,i} = \frac{b_{ta,i} - b_{ab,i}}{b_{ab,i}} = \frac{b_{ta,i} - a/\sqrt{2}}{a_0/\sqrt{2}} = \frac{\sqrt{2}}{a_0}b_{ta,i} - 1 \tag{8}$$

represents the average strain of atomic bonds of a given atom i as seen by its nearest neighbors lying on the plane described by the normal versor $\hat{n}$. Finally, from the MD simulation it is straightforward to calculate the atomic displacement distributions for couples of atoms at distance L; this way the Warren's plot ($\sqrt{\overline{\Delta L^2_{hkl}(L)}}$ *vs* L) can be obtained along any desired [hkl] scattering direction,[29] and compared with the corresponding result of the modelling of the experimental powder diffraction pattern.

IV. CONCLUSION

Pd nanocubes produce a newly observed pattern of interference fringes, accessible by high resolution X-ray powder diffraction because the measured nanocrystals are nearly homogeneous in shape and size. This observation is analogous to information typically obtained from larger crystals – and with considerable experimental complexity – by coherent X-ray diffraction, with the significant advantage of simultaneously considering information from a large set of crystallographic directions, for a billion-sized population of nanocrystals. These XRPD data, exploited by suitable data modeling, give access to detailed information of nanocrystal size, shape, and a complex atomic displacement caused by surface forces. Consequently, XRPD can be considered as an imaging probe. The excellent match between

diffraction and molecular dynamics provides a strong experimental validation of MD simulations, previously absent in the literature. MD predictions can then be reliably used to further speculate about the nature of strain in metal nanocrystals. We reveal a nanocrystal size and shape dependence of surface strain, the most significant finding here being the non-uniform distribution of atomic distances across the different exposed facets. The strain pattern and the way it changes for diffraction sizes, shapes, and positions on each facet, could be the key to further understand the catalytic behavior of shaped nanocrystals.

ACKNOWLEDGMENTS

Use of the Advanced Photon Source at Argonne National Laboratory was supported by the U.S. Department of Energy, Office of Science, Office of Basic Energy Sciences, under Contract No. DE-AC02-06CH11357.

---

* Paolo.Scardi@unitn.it

[1] Z. Ma and F. Zaera, *Encyclopedia of Inorganic Chemistry* (John Wiley & Sons, Ltd, 2006).

[2] T. Ahmadi, Z. Wang, T. Green, A. Henglein, and M. El-Sayed, Science **272**, 1924 (1996).

[3] H. Lee, S. Habas, S. Kweskin, D. Butcher, G. Somorjai, and P. Yang, Angewandte Chemie **118**, 7988 (2006).

[4] N. Tian, Z.-Y. Zhou, S.-G. Sun, Y. Ding, and Z. L. Wang, Science **316**, 732 (2007).

[5] I. Lee, F. Delbecq, R. Morales, M. A. Albiter, and F. Zaera, Nature Materials **8**, 132 (2009).

[6] M. Jin, H. Zhang, Z. Xie, and Y. Xia, Energy & Environmental Science **5**, 6352 (2012).

[7] M. Laskar and S. E. Skrabalak, ACS Catalysis **4**, 1120 (2014).

[8] K. M. Bratlie, H. Lee, K. Komvopoulos, P. Yang, and G. A. Somorjai, Nano Letters **7**, 3097 (2007).

[9] C.-K. Tsung, J. N. Kuhn, W. Huang, C. Aliaga, L.-I. Hung, G. A. Somorjai, and P. Yang, Journal of the American Chemical Society **131**, 5816 (2009).

[10] A. Nilsson, L. Pettersson, B. Hammer, T. Bligaard, C. Christensen, and J. Nørskov, Catalysis Letters **100**, 111 (2005).

[11] J. K. Nørskov, T. Bligaard, J. Rossmeisl, and C. H. Christensen, Nature Chemistry **1**, 37 (2009).

[12] S. J. Hwang, S.-K. Kim, J.-G. Lee, S.-C. Lee, J. H. Jang, P. Kim, T.-H. Lim, Y.-E. Sung, and S. J. Yoo, Journal of the American Chemical Society **134**, 19508 (2012).

[13] H. Xin and S. Linic, The Journal of Chemical Physics **132**, 221101 (2010).

[14] T. H. Yu, T. Hofmann, Y. Sha, B. V. Merinov, D. J. Myers, C. Heske, and W. A. Goddard, The Journal of Physical Chemistry C **117**, 26598 (2013).

[15] J. Wang, Q. Wang, X. Jiang, Z. Liu, W. Yang, and A. I. Frenkel, The Journal of Physical Chemistry C **119**, 854 (2015), http://dx.doi.org/10.1021/jp510730a.

[16] M. Scott, C.-C. Chen, M. Mecklenburg, C. Zhu, R. Xu, P. Ercius, U. Dahmen, B. Regan, and J. Miao, Nature **483**, 444 (2012).

[17] K. W. Urban, Science **321**, 506 (2008).

[18] S. J. L. Billinge and I. Levin, Science **316**, 561 (2007).

[19] D. Wang, H. L. Xin, R. Hovden, H. Wang, Y. Yu, D. A. Muller, F. J. DiSalvo, and H. D. Abruña, Nature Materials **12**, 81 (2013).

[20] C.-C. Chen, C. Zhu, E. R. White, C.-Y. Chiu, M. C. Scott, B. C. Regan, L. D. Marks, Y. Huang, and J. Miao, Nature **496**, 74 (2013).

[21] V. Ortalan, A. Uzun, B. C. Gates, and N. D. Browning, Nature Nanotechnology **5**, 843 (2010).

[22] N. Shibata, S. J. Pennycook, T. R. Gosnell, G. S. Painter, W. A. Shelton, and P. F. Becher, Nature **428**, 730 (2004).

[23] C. Cui, L. Gan, M. Heggen, S. Rudi, and P. Strasser, Nature Materials **12**, 765 (2013).

[24] W. J. Huang, R. Sun, J. Tao, L. D. Menard, R. G. Nuzzo, and J.-M. Zuo, Nature Materials **7**, 308 (2008).

[25] S. I. Sanchez, M. W. Small, E. S. Bozin, J.-G. Wen, J.-M. Zuo, and R. G. Nuzzo, ACS Nano **7**, 1542 (2013).

[26] I. K. Robinson, Journal of the Physical Society of Japan **82**, 021012 (2013).

[27] M. Jin, H. Liu, H. Zhang, Z. Xie, J. Liu, and Y. Xia, Nano Research **4**, 83 (2011).

[28] W. Cha, S. Song, N. C. Jeong, R. Harder, K. B. Yoon, I. K. Robinson, and H. Kim, New Journal of Physics **12**, 035022 (2010).

[29] A. Leonardi, M. Leoni, S. Siboni, and P. Scardi, Journal of Applied Crystallography **45**, 1162 (2012).

[30] B. E. Warren and B. L. Averbach, Journal of Applied Physics **21**, 595 (1950).

[31] N. Bhattarai, G. Casillas, S. Khanal, J. Salazar, A. Ponce, and M. Jose-Yacaman, Journal of Nanoparticle Research **15**, 1660 (2013).

[32] C.-H. Kuo, L. K. Lamontagne, C. N. Brodsky, L.-Y. Chou, J. Zhuang, B. T. Sneed, M. K. Sheehan, and C.-K. Tsung, ChemSusChem **6**, 1993 (2013).

[33] P. Strasser, S. Koh, T. Anniyev, J. Greeley, K. More, C. Yu, Z. Liu, S. Kaya, D. Nordlund, H. Ogasawara, M. F. Toney, and A. Nilsson, Nat Chem **2**, 454 (2010).

[34] M. Oezaslan, F. Hasché, and P. Strasser, The Journal of Physical Chemistry Letters **4**, 3273 (2013).

[35] N. Semagina, A. Renken, and L. Kiwi-Minsker, The Journal of Physical Chemistry C **111**, 13933 (2007).

[36] S. Kaya, D. Friebel, H. Ogasawara, T. Anniyev, and A. Nilsson, Journal of Electron Spectroscopy and Related Phenomena **190, Part A**, 113 (2013).

[37] P. Scardi, in *Powder diffraction: theory and practice* (The Royal Chemistry Society: Cambridge, 2008) Chap. 13, pp. 376–413.

[38] K. R. Beyerlein, R. L. Snyder, M. Li, and P. Scardi, Journal of Nanoscience and Nanotechnology **12**, 8554 (2012).

[39] N. C. Popa, Journal of Applied Crystallography **31**, 176 (1998).

[40] T. Adler and C. R. Houska, Journal of Applied Physics **50**, 3282 (1979).

[41] I. C. Noyan and J. B. Cohen, *Residual stress. Measurement by diffraction and interpretation* (Springer-Verlag, 1987).

[42] Actually, the Goodness of Fit improves, *i.e.* decreases, when A and S_1 are fixed, as the small increase in weighted sum of squares is offset by the effect of using (2) less free parameters.

[43] S. Plimpton, Journal of Computational Physics **117**, 1 (1995).

[44] M. S. Daw and M. I. Baskes, Phys. Rev. Lett. **50**, 1285 (1983).

[45] M. S. Daw and M. I. Baskes, Phys. Rev. B **29**, 6443 (1984).

[46] H. W. Sheng, M. J. Kramer, A. Cadien, T. Fujita, and M. W. Chen, Physical Review B **83**, 134118 (2011).

[47] T. Schneider and E. Stoll, Phys. Rev. B **17**, 1302 (1978).

[48] W. Shinoda, M. Shiga, and M. Mikami, Phys. Rev. B **69**, 134103 (2004).